An ultrasensitive multimodal intracranial pressure biotelemetric system enabled by exceptional point and iontronics

Supplementary Material

SM Note 1: Eigenfrequencies of a standard second-order PT-symmetric oscillator with asymmetric capacitive perturbations

Considering the circuit diagram shown in Fig. S1a, which is formed by an active oscillator as the reader ($-R_1$, L_1, C_1) and a passive oscillator as the sensor (R_2, L_2, C_2), one can apply Kirchhoff's laws to such an electronic circuit and write the circuit dynamics as

$$\begin{cases} i\omega\left(L_1 I_1 + M_{12} I_2\right) - I_1 R_1 + \dfrac{I_1}{i\omega C_1} = 0 \\ i\omega\left(L_2 I_2 + M_{21} I_1\right) + I_2 R_2 + \dfrac{I_2}{i\omega C_2} = 0 \end{cases}, \tag{1}$$

where I_1 and I_2 are the currents of the reader and sensor, respectively. We can then recast the above equation to the following matrix form as

$$\begin{pmatrix} i\omega L_1 - R_1 + \dfrac{1}{i\omega C_1} & i\omega M_{12} \\ i\omega M_{21} & i\omega L_2 + R_2 + \dfrac{1}{i\omega C_2} \end{pmatrix} \begin{pmatrix} I_1 \\ I_2 \end{pmatrix} = 0, \tag{2}$$

which can be then simplified to

$$\begin{pmatrix} i - \dfrac{\omega_1}{\omega}\dfrac{1}{\gamma_1} - i\dfrac{\omega_1^{\,2}}{\omega^2} & i\mu_{12} \\ i\mu_{12} & i + \dfrac{\omega_2}{\omega}\dfrac{1}{\gamma_2} - i\dfrac{\omega_2^{\,2}}{\omega^2} \end{pmatrix} \begin{pmatrix} I_1 \\ I_2 \end{pmatrix} = 0. \tag{3}$$

Here $\gamma_{1,2} = R_{1,2}^{-1}\sqrt{L_{1,2}/C_{1,2}}$ is the non-Hermiticity parameter of this non-Hermitian system, $\mu_{12,21} = M_{12,21}/\sqrt{L_1 L_2}$ denotes the inductive coupling strength and $M_{12,21}$ is the mutual inductance between two coils.

In the weak coupling regime, the equation can be described approximately by the temporal coupled-mode equations[1] with $I_{1,2} = I_n^0 e^{-i\omega t}$. By making the approximation[2] of $\mu_{12,21} \ll 1$ and $1 - \dfrac{\omega_0^{\,2}}{\omega^2} \approx \dfrac{2(\omega - \omega_0)}{\omega_0}$, we have

$$H_0 \boldsymbol{I}_{\boldsymbol{n}}^{\boldsymbol{0}} = \omega_n^0 \boldsymbol{I}_{\boldsymbol{n}}^{\boldsymbol{0}}, \tag{4}$$

and the two-level PT-symmetric Hamiltonian can be written as

$$H_0 = \begin{pmatrix} 1 - i\dfrac{1}{2\gamma_1} & -\dfrac{\mu_{12}}{2} \\ -\dfrac{\mu_{21}}{2} & 1 + i\dfrac{1}{2\gamma_2} \end{pmatrix}. \tag{5}$$

Thus, its normalized eigenfrequencies can be expressed as

$$\omega_{1,2} = 1 + i\left(\frac{1}{4\gamma_2} - \frac{1}{4\gamma_1}\right) \pm \frac{1}{4\gamma_1\gamma_2}\sqrt{4\mu_{12}\mu_{21}\gamma_1{}^2\gamma_2{}^2 - (\gamma_1 + \gamma_2)^2}. \tag{6}$$

The PT symmetry condition requires that $\left[PT,\, H_0\right] \equiv PT\, H_0 - H_0\, PT = 0,$ leading to $\gamma_1 = \gamma_2 = \gamma$ and $\mu_{12} = \mu_{21} = \mu$; here, P denotes the parity operator associated with the first Pauli matrix and T is the timer-reversal operator which takes the complex conjugation. Then, the eigenfrequencies in the unit of the resonance frequency ($\omega_0 = 1/\sqrt{LC}$) yield

$$\omega_{1,2} = 1 \pm \frac{1}{2\gamma}\sqrt{\mu^2\gamma^2 - 1}. \tag{7}$$

The exact solution of eigenfrequencies in the PT-symmetric electronic system, as a function of γ and the coupling strength μ, has been given by ref. [3], and has the form of

$$\omega_{1,2} = \pm\sqrt{\frac{2\gamma^2 - 1 \pm \sqrt{1 - 4\gamma^2 + 4\gamma^4\mu^2}}{2\gamma^2\left(1 - \mu^2\right)}}. \tag{8}$$

Figure S2 demonstrates that the exact solution and the approximation of eigenfrequencies can have a perfect agreement with each other when $\mu < 0.1$.

Considering the tiny capacitance variation ($C_2' = C_2 + \Delta C$) introduced to the sensor end only, the equation can be rewritten as

$$\begin{cases} i\omega\left(L_1 I_1 + M_{21} I_2\right) - I_1 R_1 + \dfrac{I_1}{i\omega C_1} = 0 \\ i\omega\left(L_2 I_2 + M_{12} I_1\right) + I_2 R_2 + \dfrac{I_2}{i\omega\left(C_2 + \Delta C\right)} = 0 \end{cases}. \tag{9}$$

Defining $\delta = \Delta C / C << 1$, the equation is given by

$$\begin{pmatrix} i - \dfrac{\omega_0}{\omega}\dfrac{1}{\gamma} - i\dfrac{\omega_0{}^2}{\omega^2} & i\mu \\ i\mu & i + \dfrac{\omega_0}{\omega}\dfrac{1}{\gamma} - i\dfrac{\omega_0{}^2}{\omega^2}\dfrac{1}{1+\delta} \end{pmatrix} \begin{pmatrix} I_1 \\ I_2 \end{pmatrix} = 0. \tag{10}$$

We make the approximation $\dfrac{1}{1+\delta} \approx 1-\delta$, the effective Hamiltonian H' is obtained

$$H' = \begin{pmatrix} 1 - i\dfrac{1}{2\gamma} & -\dfrac{\mu}{2} \\ -\dfrac{\mu}{2} & 1 - \dfrac{\delta}{2} + i\dfrac{1}{2\gamma} \end{pmatrix}. \tag{11}$$

The solution of the normalized eigenfrequency can be obtained as follows

$$\omega'_{1,2} = 1 - \frac{\delta}{4} \pm \frac{1}{4\gamma}\sqrt{(\delta^2 + 4\mu^2)\gamma^2 - 4i\delta\gamma - 4}. \tag{12}$$

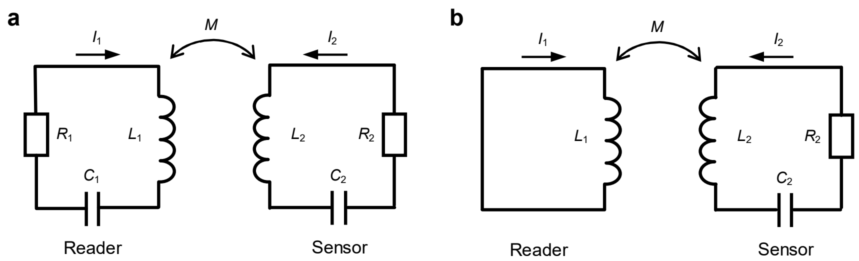

FIG. S1. The equivalent circuit diagram of (a) the PT-symmetric system and (b) the conventional "LC" wireless system.

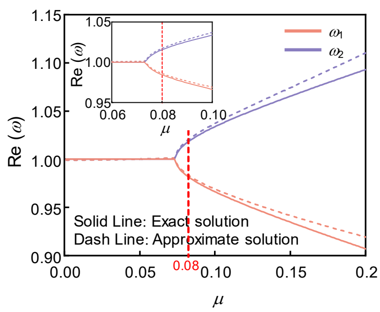

Fig. S2. The exact and approximate solutions of the real part $\text{Re}(\omega)$ of the eigenvalues as a function of the coupling coefficient μ.

SM Note 2: Eigenfrequencies of a conventional "LC" system

Considering the circuit diagram shown in Fig. S1b above, which is formed by a reader (L_1) and a sensor (L_2, C_2, R_2). One can apply Kirchhoff's laws to such an electronic circuit and write the circuit dynamics as

$$\begin{cases} i\omega\left(L_1 I_1 + M_{12} I_2\right) = 0 \\ i\omega\left(L_2 I_2 + M_{21} I_1\right) + I_2 R_2 + \dfrac{I_2}{i\omega C_2} = 0 \end{cases}. \tag{13}$$

Thus, its eigenfrequencies for conventional LC system can be expressed as

$$\omega_{\mathrm{LC}1,2} = \frac{i(C_2 R_2 \pm \sqrt{C_2{}^2 R_2{}^2 + 4L_2 C_2 \mu^2 - 4L_1 C_2})}{C_2(L_1 - L_2\mu^2)}. \tag{14}$$

Substituting $L_1 = L_2$, $\mu = M_{12,21} / \sqrt{L_1 L_2} = M / L$, $\gamma_2 = R_2^{-1}\sqrt{L_2 / C_2}$ to make fair comparison with the EP system, the solution of the normalized eigenfrequencies can be obtained as follow

$$\omega_{\mathrm{LC}1,2} = \frac{1}{2\gamma(1-\mu^2)}(i \pm \sqrt{4\gamma^2(1-\mu^2) - 1}). \tag{15}$$

Considering the tiny capacitance variation introduced to the sensor end only, the eigenfrequencies can be rewritten as

$$\omega_{\mathrm{LC}1,2}{}' = \frac{1}{2\gamma\sqrt{1+\delta}(1-\mu^2)}(i \pm \sqrt{4\gamma^2(1+\delta)(1-\mu^2) - 1}). \tag{16}$$

SM Note 3: The enlarged cross-sectional view of microstructures obtained by SEM

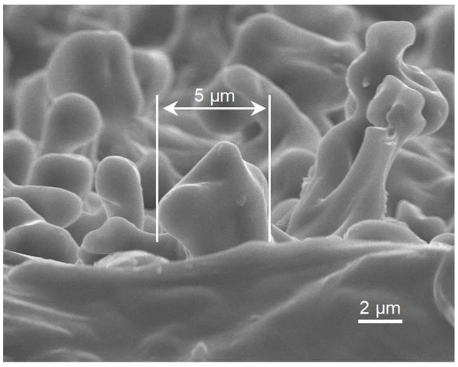

FIG. S3. The enlarged cross-sectional SEM image of a PVA/H_3PO_4 film. Similar result can be repeated for at least five times.

SM Note 4: Voltage divider circuit for response time measurement

To determine the response times of the transducer, we construct a voltage divider circuit and utilized a high-speed oscilloscope for precise measurements. As depicted in Fig. S4, a 24 MHz AC signal is generated and applied to the transducer via a signal generator, while pressure is exerted on the transducer by a dynamometer. It converts the capacitance change into voltage variations. Due to its exceptionally high sampling rate (maximum 16 GSa/s), high-speed oscilloscopes are capable of easily capturing voltage fluctuations derived from the transducer.

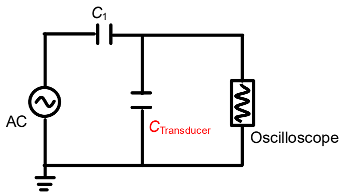

FIG. S4. The Schematic of the voltage divider circuit.

SM Note 5: Responses of the transducer against the pressure variations

External perturbations to the PT-symmetric systems typically induce asymmetry predominantly on the sensor side. For optimal sensing, the PT-symmetric system is generally tuned to the exact phase. Variations within the sensor introduce asymmetry, causing the system to deviate from its PT-symmetric state and resulting in a detectable frequency shift. The implementation of this method is straightforward and robust to external variations.

An iontronic pressure transducer is employed in the EP-based biotelemetric system for the wireless monitoring of ICP, and it can be treated as a parallel connection of capacitance (C_P) and resistance (R_P). The relationship between the capacitance and resistance of the iontronic transducer as a function of pressure can be found in Fig. S5a; it exhibits a large impedance variation. The real part of impedance can be written as $\mathrm{Re}(Z_{\mathrm{in}}) = \dfrac{R_P}{1+(\omega R_P C_P)^2}$. However, when the iontronic pressure transducer is connected in parallel with a capacitor ($C_2 = 20\ \mathrm{pF}$), the resultant equivalent impedance is nearly negligible as depicted in Fig. S5b. This configuration significantly diminishes the impact of resistance variations on the impedance. Fig. S5c examines the influence of parallel capacitance on the frequency offset within the system, clearly demonstrating that the effects of the resistance are substantially reduced. As evidenced in Fig. S5d, it has negligible effects on frequency offset in comparison to the capacitance effects. Consequently, the iontronic pressure transducer is predominantly characterized as a capacitive element when its resistance is disregarded through the parallel connection of a capacitor.

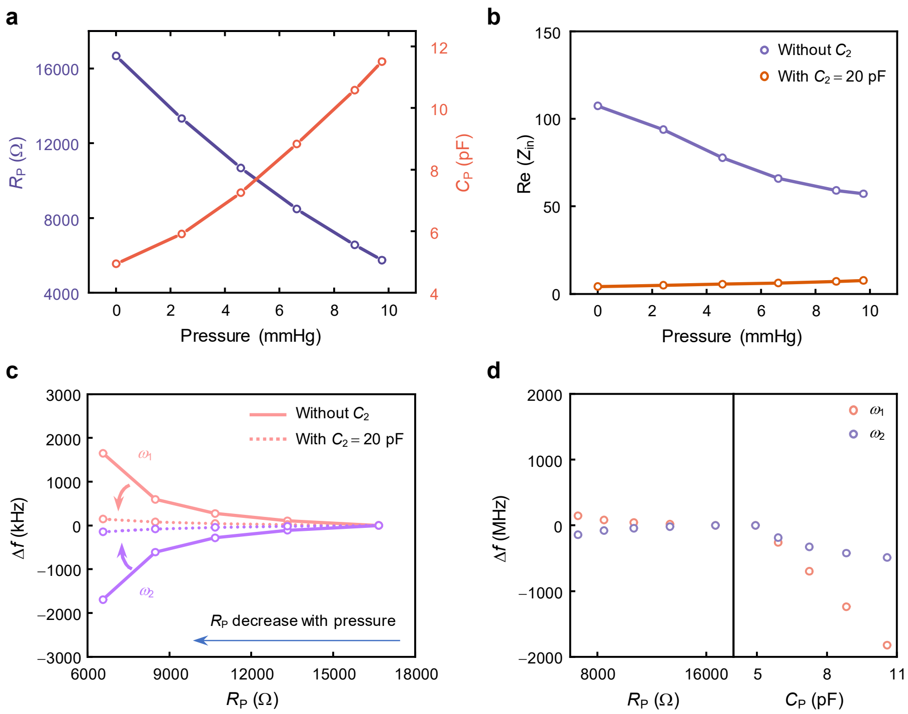

FIG. S5. (a) Resistance and capacitance of the iontronic transducer as a function of applied pressure. (b) The real part of the impedance $\mathrm{Re}(Z_{\mathrm{in}})$ change for the ICP transducer with/without $C_2 = 20\ \mathrm{pF}$. (c) Dependency of the system frequency offset on the transducer's resistance. (d) With a parallel 20pF capacitor, system frequency offset as a function of the transducer's resistance and capacitance, respectively.

SM Note 6: A summary of state-of-the-art pressure monitoring systems

Table S1. Pressure monitoring systems performance summary

Measuring range	Size (mm)	Operating frequency	Pressure sensitivity	Resolution	Ref
0 – 100	2.5 × 2.5	~5 GHz	~1.084 MHz/mmHg	0.2 mmHg	[4]
5 – 50	10 × 10	4.1 GHz	2.64 MHz/mmHg	…	[5]
5 – 50	14 × 14	~3.8 GHz	1.28 MHz/mmHg	…	[6]
0 – 30	8 × 8	~260 MHz	~200 kHz/mmHg	1 mmHg	[7]
0 – 120	60 × 70	~13.56 MHz	160 Hz/mmHg	…	[8]
0 – 40	5 × 5	35 MHz ~ 2.7 GHz	0.92 MHz/mmHg	0.028 mmHg	[9]
0 – 10	10 × 10	24 MHz	115.95 kHz/mmHg	0.003 mmHg	This work

SM Note 7: Detail analysis of noise

The exceptional point (EP)-based sensors do enhance the sensitivity but provide no fundamental signal-to-noise ratio (SNR) enhancement[10]. That is said, while the system has enhanced responsivity towards the target perturbations around EP, any unwanted noise existing in the system will also be amplified in the same magnitude. Therefore, to benefit from the sensitivity enhancement brought by the EP, any unwanted noise of the sensing system should be suppressed to be sufficiently small compared to the target perturbation.

Generally, there are several noise sources in electromagnetic systems, such as shot noise, flicker noise, thermal noise, and quantum noise. Particularly, quantum noise originated from the quantization nature of charged carriers and photons is significant in optical and photonic systems[11], but can be ignored in our radio-frequency EP sensing system. Shot noise and flicker ($1/f$ noise) exist in solid-state devices and vacuum electronics, which are important only at low frequencies (i.e., 1 Hz to 1 MHz). Consequently, thermal noise (Johnson-Nyquist noise[12]) sourced from the thermal agitation of bounded charges in devices (especially in resistors), which simultaneously introduces the resonance frequency shifts, is considered the dominant noise source in this work.

According to the Planck's black body radiation law, electrons in a real-world resistor are in random motion, whose kinetic energy may produce small, random voltage fluctuations across this resistor with a zero average but a nonzero root mean square (RMS) value, which can be expressed as

$$\overline{V}_{\text{nosie}} = \sqrt{\frac{4hfBR}{e^{hf/kT}-1}}, \tag{17}$$

where h denotes the Planck's constant, k is the Boltzmann's constant, T represents the temperature in kelvin, $f(B)$ is the center frequency (bandwidth), and R is the resistance value. In the low frequency range where the approximation $hf \ll kT$ takes account, the above equation can be simplified to $\overline{V}_{\text{nosie}} = \sqrt{4kTBR}$. This indicates that the noise voltage fluctuates between $\pm\sqrt{8kTBR}$. Therefore, the voltage across a non-ideal resistor can be decomposed into $V' = V_R + V_{\text{noise}}$, as seen in Fig. S6a. This model can also be equivalent to the series connection of an ideal resistor (R) and a noisy resistor (R'), as seen in Fig. S6b, such that $V' = I(R+R') = IR + IR' = V_R + V_{\text{noise}}$. Defining a time-fluctuating parameter $\varepsilon_{1,2} = R'/R$ where the subscript 1,2 denotes the deviation occurring to the resistors of the gain or loss oscillator, we can analyze the resonance frequency fluctuations due to thermal noise. Here, to simplify our analysis, we assume $\varepsilon_{1,2} \in [-\Delta, \Delta]$ where $\Delta \propto \sqrt{8kTB/R}$.

In experiments, the measurement of eigenfrequencies associated with the Hamiltonians is realized by tracking the dips of reflection spectra, which, in this work, is the reflection coefficient (S_{11}) at the gain side (Fig. S6c). The noise-deviated S_{11}, considering the maximum noise ($\varepsilon_{1,2} \equiv \Delta$), has the form of

$$S_{11} = \frac{\eta(1+\Delta)^2\omega^2 + \eta\gamma^2[1-2\omega^2-(\mu^2-1)\omega^4]}{[(1+\Delta)(\eta+\Delta\eta)-2\omega^2] - 2i\gamma\omega(\omega^2-1) + \eta\gamma^2[1-2\omega^2-(\mu^2-1)\omega^4]}, \tag{18}$$

which yields the maximized deviated resonance frequency to be

$$\omega_{1,2}' = \sqrt{\frac{(1+\Delta)^2 - 2\gamma^2 \pm \sqrt{(1+\Delta)^4 - 4\gamma^2(1+\Delta)^2 + 4\gamma^4\mu^2}}{2\gamma^2(\mu^2-1)}}. \tag{19}$$

The frequency fluctuation caused by the noise is $\Delta\omega = \omega_{1,2} - \omega_{1,2}'$. Taking parameters used in our experiments (e.g., $\gamma = 13.56$, $\mu = 0.08$ and the system operates at $f_0 \approx 24.1$ MHz and $T = 290$ K), the above equation yields $\Delta f = \Delta\omega / 2\pi \approx 1$ kHz, which agrees well with our noise measurements in Fig. S6d that the measured frequency may have ± 2.5 kHz fluctuation. This noise-introduced frequency fluctuation is indeed ignorable compared to the frequency shift caused by the target pressure variations (~ 10 – ~ 400 kHz), which, therefore, does not negate the implementation of the EP for sensing.

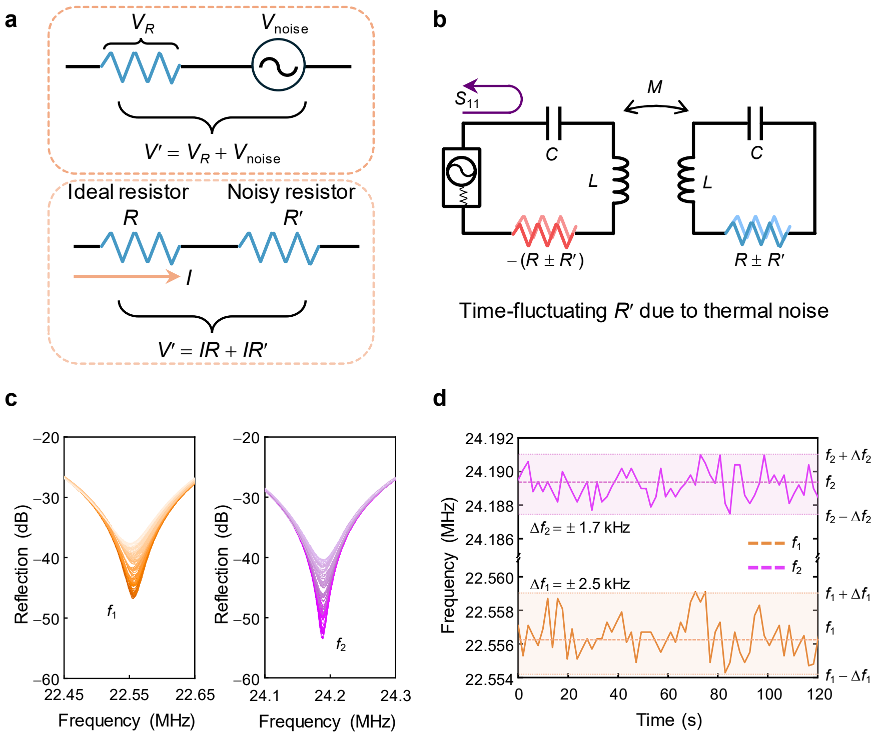

Fig. S6. (a) Circuit equivalent of a non-ideal resistor. (b) Circuit diagram of the EP sensing system considering the presence of thermal noise. (c) Reflection spectra measured within 120 seconds (~ per 2 seconds) without perturbations applied. (d) Frequency fluctuations caused by the noise.

SM Note 8: Comparison of sensing distance between PT symmetry system and conventional “LC” wireless sensing

The relationship between the wireless coupling distance of two coils and the coupling coefficient is illustrated in Fig. S7a. Figures. S7b and S7c present a comparative analysis of the reflection spectra between the PT-symmetric system and the conventional wireless “LC” system versus coupling distance. The PT-symmetric system is characterized by its sharply defined resonance peaks with substantial amplitudes, crucial for detecting minute physiological variations. Its ability to maintain sharp resonances, even with varying coupling coefficients, underscores its robust stability and superior precision monitoring capabilities. In the PT-exact phase, the system achieves maximum resolution. As the coupling distance increases (μ decreases), the system transitions from the exact state to the broken state, during which the two eigenfrequencies converge and the amplitude of the reflection peak progressively diminishes. The degree, to which these peaks are pronounced, correlates with the system’s potential for exceptional sensitivity and accuracy in detecting the changes it is tuned to monitor.

The resonant frequency obtained from the reflection spectrum (red point in Fig. S7c) is written as: $\omega_c = \sqrt{1/[(1-\mu^2)L_2C_2]}$. It is worth noting that the intensity of conventional “LC” system reflectance spectra decreases sharply with increasing coupling distance, making it difficult to observe at the detection distance of ICP. The conventional wireless “LC” systems show disappointing resolution, with significantly low S_{11} amplitude and gradually disappear as the coupling coefficient decreases. This decreased resolution in the conventional “LC” system is a result of its inherent energy dissipation characteristics, which lead to broader spectral responses and thus a reduced ability to precisely pinpoint specific resonant frequencies. This means that at the detection distance of the ICP, it is not able to fulfill the requirement of discerning small variations in monitored parameters—such as intracranial pressure.

The PT-symmetric system’s superior detection and response capabilities render it highly effective for monitoring applications, particularly in biotelemetry, where precise detection of small physiological changes is paramount. The pronounced difference in the resonance peak sharpness between the PT-symmetric and convention LC systems highlights the former’s superior performance, underscoring its potential for groundbreaking advancements in non-invasive medical monitoring technologies.

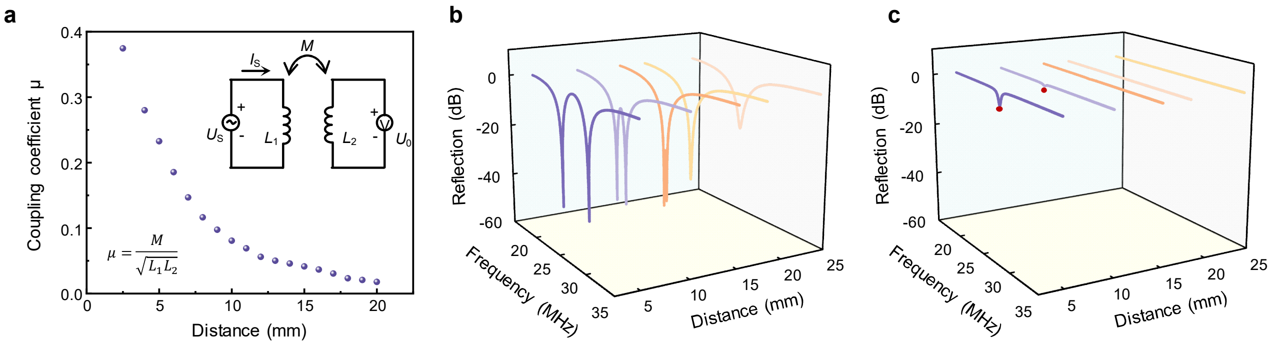

FIG. S7. (a) Coupling coefficient as a function of the wireless coupling distance of the two coils. (b) Magnitude of the reflection coefficient for the (b) PT-symmetric system and (c) conventional "LC" wireless system, under varying coupling distance.

SM Note 9: Photograph of the sensor

FIG. S8. Photograph of the sensor.

SM Note 10: Frequency response of the sensor system under low pressure

As mentioned in SM note 7, we have both theoretically and experimentally demonstrated that the noise-induced frequency fluctuations are within ± 2.5 kHz, which can be ignored compared to the eigenfrequency shift caused by the target pressure variations. To demonstrate that the fluctuations in Fig. 5g in the main text are induced by the heartbeat signal instead of noise, we further perform experiments in the low-pressure range (0 - 0.15 mmHg) shown in Fig. S9. The results demonstrate that the noise-induced (no pressure applied) frequency fluctuations (marked in Fig. S9a and zoomed-in in Fig. S9b) are below 2 kHz, while the frequency fluctuations caused by the heartbeat signal is ~ 25 kHz (the grey area marked in Fig. S9a), which is more than one order of magnitude larger than the noise-induced fluctuation (Fig. S9b). In addition, the results in Fig. 4f, which demonstrates clear frequency differentiation under extremely weak pressure perturbations, further support this finding. Figure 5g shows that the frequency fluctuation caused by the heartbeat is about 25 kHz, significantly greater than that caused by noise. The fast Fourier transformation (FFT) analysis (Fig. S9c) of the ICP signal from Fig. 5f reveals two distinct peaks: one for breathing (~ 0.33 Hz) and another for heartbeat (~ 3.76 Hz), which closely matches the ECG results.

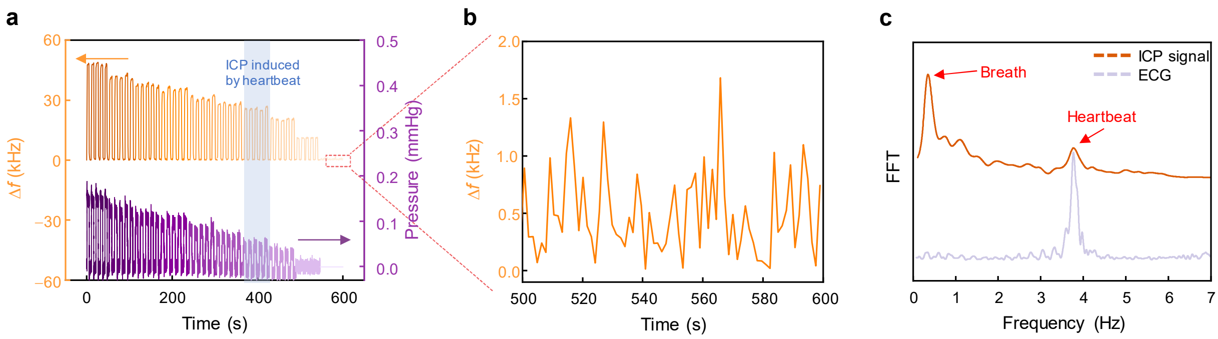

Fig. S9. (a) Frequency shift of ω_2 in response to low applied pressure (~ per 60 seconds). (b) Enlarged view of frequency shift without applied pressure. (c) FFT analysis of ICP signal and ECG.

Supplementary References

1. Park, S., Lee, J. & Kim, S. Robust Wireless Power Transfer with Minimal Field Exposure Using Parity-Time Symmetric Microwave Cavities. *Phys. Rev. Appl.* **16**, 014022 (2021).

2. Zhou, B. Bin, Wang, L. F., Dong, L. & Huang, Q. A. Observation of the perturbed eigenvalues of PT-symmetric LC resonator systems. *J. Phys. Commun.* **5**, 045010 (2021).

3. Chen, P.-Y. *et al.* Generalized parity–time symmetry condition for enhanced sensor telemetry. *Nat. Electron.* **1**, 297–304 (2018).

4. Chen, L. Y. *et al.* Continuous wireless pressure monitoring and mapping with ultra-small passive sensors for health monitoring and critical care. *Nat. Commun.* **5**, 5028 (2014).

5. Kim, J. *et al.* Wearable smart sensor systems integrated on soft contact lenses for wireless ocular diagnostics. *Nat. Commun.* **8**, 14997 (2017).

6. Yang, C. *et al.* Intelligent wireless theranostic contact lens for electrical sensing and regulation of intraocular pressure. *Nat. Commun.* **13**, 2556 (2022).

7. Lu, D. *et al.* Bioresorbable Wireless Sensors as Temporary Implants for In Vivo Measurements of Pressure. *Adv. Funct. Mater.* **30**, 2003754 (2020).

8. Nikbakhtnasrabadi, F., Hosseini, E. S., Dervin, S., Shakthivel, D. & Dahiya, R. Smart Bandage with Inductor-Capacitor Resonant Tank Based Printed Wireless Pressure Sensor on Electrospun Poly-L-Lactide Nanofibers. *Adv. Electron. Mater.* **8**, 2101348 (2022).

9. Wang, F. *et al.* A Novel Intracranial Pressure Readout Circuit for Passive Wireless LC Sensor. *IEEE Trans. Biomed. Circuits Syst.* **11**, 1123–1132 (2017).

10. Loughlin, H. & Sudhir, V. Exceptional-Point Sensors Offer No Fundamental Signal-to-Noise Ratio Enhancement. *Phys. Rev. Lett.* **132**, 243601 (2024).

11. Xiao, Z., Li, H., Kottos, T. & Alù, A. Enhanced Sensing and Nondegraded Thermal Noise Performance Based on P T-Symmetric Electronic Circuits with a Sixth-Order Exceptional Point. *Phys. Rev. Lett.* **123**, 213901 (2019).

12. Nyquist, B. H. Thermal agitation of electric charge in conductors. *Phys. Rev.* **32**, 110 (1928).